



# Projectile fragment emission in the fragmentation of $^{56}\text{Fe}$ on Al, C, and $\text{CH}_2$ targets

Luo-Huan Wang<sup>1</sup> · Liang-Di Huo<sup>1</sup> · Jia-Huan Zhu<sup>1</sup> · Hai-Rui Duan<sup>1</sup> ·  
Jing-Ya Wu<sup>1</sup> · Hui-Ling Li<sup>1</sup> · Jun-Sheng Li<sup>1</sup> · S. Kodaira<sup>2</sup> · N. Yasuda<sup>3</sup> ·  
Dong-Hai Zhang<sup>1</sup>

Received: 7 September 2019 / Revised: 7 October 2019 / Accepted: 13 October 2019 / Published online: 24 November 2019  
© China Science Publishing & Media Ltd. (Science Press), Shanghai Institute of Applied Physics, the Chinese Academy of Sciences, Chinese Nuclear Society and Springer Nature Singapore Pte Ltd. 2019

**Abstract** The emission angle distribution of projectile fragments (PFs) and the temperature of PF emission sources for fragmentation of  $^{56}\text{Fe}$  on polyethylene, carbon, and aluminum targets at the highest energy of 497 A MeV are investigated on the basis of corrected data, using a CR-39 plastic nuclear track detector. It is found that the average emission angle of PFs increases with the decrease in PF charge for the same target, and no obvious dependence of angular distribution on the mass of the target nucleus is found for the same PF. The cumulative squared transverse momentum distribution of PFs can be well represented by a single Rayleigh distribution. The temperature of PF emission sources is extracted from the distribution, and it is about 1.0–8.0 MeV and does not depend on the mass of the target for PFs with charges of  $9 \leq Z \leq 25$ .

**Keywords** Heavy-ion collision · Projectile fragmentation · Nuclear temperature · CR-39 plastic nuclear track detector

This work was supported by the National Natural Science Foundation of China (Nos. 11075100 and 11565001), the Natural Foundation of Shanxi Province (No. 2011011001-2), and the Shanxi Provincial Foundation for Returned Overseas Chinese Scholars, China (No. 2011-058).

✉ Dong-Hai Zhang  
zhangdh@sxnu.edu.cn

<sup>1</sup> Institute of Modern Physics, Shanxi Normal University, Linfen 041004, China

<sup>2</sup> Radiation Measurement Research Section, National Institute of Radiological Science, Chiba 263-8555, Japan

<sup>3</sup> Research Institute of Nuclear Engineering, University of Fukui, Fukui 914-0055, Japan

## 1 Introduction

Heavy-ion collisions at intermediate and high energies are an ideal tool for producing hot nuclear matter of various densities in the laboratory and are an important source of information on the properties of nuclear matter under extreme conditions [1, 2]. Experimental studies in this field extend from the Fermi energy regime to relativistic energies. Such studies can help us understand not only the fundamental nuclear physics processes involved in nuclear fragmentation, but also their thermodynamic evolution in collisions. Multi-fragmentation is a universal phenomenon that occurs when a large amount of energy is deposited in a nucleus. At low excitation energies, the produced nuclear system can be treated as a compound nucleus [3], which decays via the evaporation of light particles or fission. However, at high excitation energies, a considerable amount of excitation energy and a slight momentum transfer are induced, possibly accompanied by compression during the initial dynamical stage of the interaction [4, 5], and the system will expand to some sub-saturation density, thereby becoming unstable and subsequently breaking up into many fragments.

One of the major points of interest in the study of intermediate and high-energy heavy-ion collisions is the understanding of multi-fragmentation phenomenon and their connection with the liquid–gas-phase transition [2]. For this, it must be assumed that at some stage in a heavy-ion collision a part of the system is in both thermodynamic equilibrium and unstable. Such a configuration is often referred to as a freeze-out configuration. The multi-fragmentation process reflects the parameters of its source, i.e., its temperature, density, and perhaps its collective flow pattern. Among these parameters, temperature is an

important thermodynamic quantity in the nuclear equation of state, and it is of broad interest in heavy-ion collisions, because the nuclear system evolves from a very high temperature to a very low one in forming the final fragments. It is very difficult to determine experimentally the temperature of hot nuclear matter in a dynamical process. There have been several nuclear thermometers proposed to extract the temperature. These include the slope of energy spectra [6–8], momentum fluctuations [9], double isotope yield ratios [10–13], and excited state distributions [14]. However, they may not be generally applicable to all circumstances, and even for a given system, the temperature values extracted from these thermometers may be quite different from each other [15]. The typical temperature extracted from isotope ratios or level population ratios is 5–8 MeV [11–13, 16], which agrees with that used in the statistical models reproducing the experimental mass yield curves. The typical slope temperature extracted from the kinetic energy spectra of PFs is about 17 MeV [8].

In our previous publications [17–19], the total charge-changing and partial projectile fragment (PF) production cross sections, the emission angle of PFs, and the temperature of the PF emission source were studied using the original uncorrected data of  $^{56}\text{Fe}$  fragmentations on Al, C, and  $\text{CH}_2$  targets. In later investigations, it was found that the CR-39 detector was not uniformly etched, as the concentration of NaOH aqueous solution was not uniform along the solution depth. Using the distribution of the average etched track areas at different detector heights in the solution, the etched track area was corrected. The corrected average etched track area is uniformly distributed in both directions of the two sides of the detector.

In this paper, the experimental results for the emission angle distribution of PFs and the temperature of the PF emission sources, obtained for fragmentations of  $^{56}\text{Fe}$  on Al, C, and  $\text{CH}_2$  targets at a highest energy of 497 A MeV, based on the corrected data, are investigated. The present experiment is the same as one of our previous publications [17–19], though the etched track area is corrected.

## 2 Experimental details

Stacks of Al, C, and  $\text{CH}_2$  targets, sandwiched between CR-39 plastic nuclear track detectors (HARZLAS TD-1, Fukui, Japan), were perpendicularly exposed to a  $^{56}\text{Fe}$  beam with an initial energy of 500 A MeV in the biology port of the HIMAC (Heavy Ion Medical Accelerator in Chiba) facility, at the Japanese National Institute of Radiological Sciences (NIRS). The beam fluence is about 2000 ions/ $\text{cm}^2$ . The configuration of the sandwiched target is shown in Fig. 1. CR-39 sheets, with dimensions of

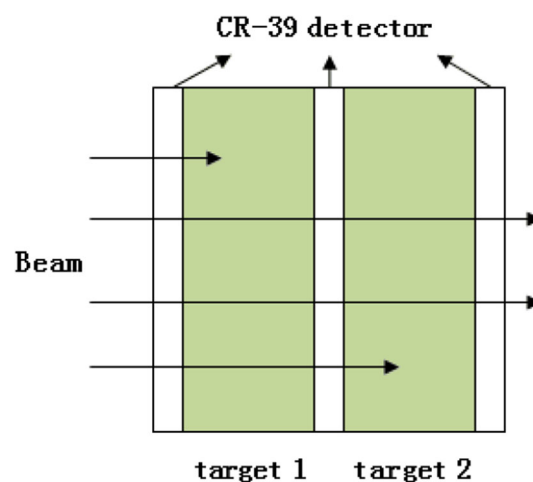


**Fig. 1** (Color online) Sketch of the target–detector configuration

5 cm  $\times$  5 cm, and thicknesses of 0.8 mm, were placed to the front and back of each target. The thicknesses of the aluminum, carbon, and polyethylene targets are 2, 5, and 10 mm, respectively. There are two targets in each stack, with one CR-39 sheet placed in front of and behind each target. The beam energy on each target's upper surface is calculated using SRIM-2008 simulation code. The beam energy on the first target's (target 1) upper surface, for each material, is 497 A MeV; on the second Al target's (target 2) upper surface, the beam energy is 478 A MeV; for the second C target's (target 2) upper surface, it is 468 A MeV; and for the second  $\text{CH}_2$  target's (target 2) upper surface, it is 462 A MeV. The accuracy of the beam energy on each target is calculated from the length uncertainty of the beam line and the uncertainty of the CR-39 sheet, which is less than 1 MeV/nucleon.

After exposure, the CR-39 detectors were etched in a 7 N NaOH aqueous solution at a temperature of 70° for 30 h. Tracks from the beam ions and their fragments are manifested in the CR-39 sheet as etch-pit cones on both sides of the sheets. The ion track images were scanned and analyzed automatically by an HSP-1000 microscope system and PitFit track measurement software and then individually checked by hand. When the track is mis-identified by the automatic PitFit track measurement process (the possible track categories include target fragment, disguised, and overlapped), the corresponding track is refitted in the manual checking process. The manual checking process is time-consuming, but it keeps the detection efficiency at 100%. The PitFit software provides geometric information for each track, including the track coordinates and major/minor axes, and the area of the etched track spot on the CR-39 sheet surfaces. About  $1.5 \times 10^4$   $^{56}\text{Fe}$  ion tracks were traced from the first CR-39 detector upper surface in the stack. The spots on the front surface (with respect to the beam direction) were directly scanned first,

and then, the sheet was rotated about its central horizontal line, and the spots on the back surface were scanned.

Trajectories of the  $^{56}\text{Fe}$  beam and the secondary projectile fragments were reconstructed in the whole stack using the track tracing method [20]. First, the track position in the CR-39 sheet surface is corrected by parallel and rotational coordinate transforms. Second, the difference between the track position of corresponding tracks on both sides of the CR-39 sheets and on the surfaces adjacent to the targets is minimized by a track matching routine.

The coordinates of the track in front of the target (or upper surface of the CR-39 sheet) are  $(x, y)$ , and coordinates of the matching track behind the target (or back surface of the CR-39 sheet) are  $(x', y')$ . Following the translation relation, the coordinates of matching tracks can be calculated as

$$\begin{aligned} x'_{\text{th}} &= ax + by + c \\ y'_{\text{th}} &= a'x + b'y + c' \end{aligned} \quad (1)$$

where  $a, b, c, a', b',$  and  $c'$  are fitting parameters, which can be fitted using the least squares method, by choosing the coordinates of at least 100  $^{56}\text{Fe}$  beam tracks. The calculated coordinates  $(x'_{\text{th}}, y'_{\text{th}})$  of the matching tracks are different from the measured  $(x', y')$ , and the differences  $dx = x'_{\text{th}} - x'$  and  $dy = y'_{\text{th}} - y'$  can be used to determine the matching tracks and to calculate the emission angles of projectile fragments and scatter angle of the beam particle.

Figure 2 shows the coordinate difference distributions of  $dx$  and  $dy$  for 497 A MeV  $^{56}\text{Fe}$  fragmentations on the  $\text{CH}_2$  target, (a) and (b) are the track coordinate differences in the upper and lower surfaces of the sheet, respectively, and (c) and (d) are the track coordinate differences in front of and behind the target, respectively; the smooth line in each figure is the Gaussian fit of the distribution. The differences are calculated for all combinations of positions of the extracted tracks; only the matched combinations ought to make a peak appear in the figures, and the  $dx$  and  $dy$  values of other combinations should be randomly distributed. The deviations ( $\sigma(dx)$  and  $\sigma(dy)$ ) give the position accuracies of tracks and are estimated to be 3.0–12.0  $\mu\text{m}$  between the upper and lower surfaces of the CR-39 sheet, and 6.0–30.0  $\mu\text{m}$  in front of and behind the targets, and they depend on the thickness of the CR-39 sheet, the type of target, and the thickness of the target. The reduction in accuracy resulting from Coulomb scattering becomes greater on the downstream detectors, because Coulomb scattering effects increase with the increase in the energy loss. However, because the matching track is searched for within a range equaling four times the deviation in our investigation, the Coulomb scattering effect is negligible.

There are several possibilities when matching tracks in the region of  $(x'_{\text{th}} \pm 4\sigma(dx), y'_{\text{th}} \pm 4\sigma(dy))$  or in the region

of projectile fragmentation angle ( $\theta_{\text{fr}} = p_f/p_{\text{beam}}$ , where  $p_f$  is the Fermi momentum of nucleons in the nuclei, which is about 200 MeV/c, and  $p_{\text{beam}}$  is the momentum of the  $^{56}\text{Fe}$ ) beam on the detector surfaces adjacent to the target. In the present experiment, we choose the region  $(x'_{\text{th}} \pm 150 \mu\text{m}, y'_{\text{th}} \pm 150 \mu\text{m})$  as a candidate track search region, which is larger than the region for the projectile fragmentation angle.

1. There is a candidate track in the region  $(x'_{\text{th}} \pm 150 \mu\text{m}, y'_{\text{th}} \pm 150 \mu\text{m})$ ; the area of the matched track is in the region of the  $^{56}\text{Fe}$  beam track area and is not considered as a fragmentation event.
2. There is a candidate track in the region  $(x'_{\text{th}} \pm 150 \mu\text{m}, y'_{\text{th}} \pm 150 \mu\text{m})$ ; the area of the matched track is less than the region of the  $^{56}\text{Fe}$  beam track area and is considered as a fragmentation event.
3. There are two or three candidate tracks in the region  $(x'_{\text{th}} \pm 150 \mu\text{m}, y'_{\text{th}} \pm 150 \mu\text{m})$ ; the sum of the matched track charge is equal to or less than the charge of the  $^{56}\text{Fe}$  beam and is also considered as a fragmentation event.
4. There is a candidate track in the region  $(x'_{\text{th}} \pm 150 \mu\text{m}, y'_{\text{th}} \pm 150 \mu\text{m})$ ; the area of the matched track is greater than the region of the  $^{56}\text{Fe}$  beam track area and is considered as a charge-pickup reaction event.
5. There is no candidate track in the region  $(x'_{\text{th}} \pm 150 \mu\text{m}, y'_{\text{th}} \pm 150 \mu\text{m})$ ; it is considered as a complete fragmentation event, but the fragment charges are less than the threshold of the CR-39 detector.

In a solid-state nuclear track detector such as the CR-39, etching of the CR-39 detector produces conical etch pits coincident with the point of penetration of the original ionizing particle in the detector. The area or minor axis of the elliptically shaped etch-pit mouth is a sensitive function of the quantity  $Z^*/\beta$  of the particle passing through it, where  $Z^*$  is the ionic effective charge and  $\beta$  is the velocity of the projectile. For projectile fragmentation on the thin target, the velocity of the projectile fragment is essentially the same as that of the projectile, and as a consequence of this, there is a monotonic relation between the charge and size or minor axis of the etch pit for either the beam nucleus or the nuclear fragment.

The charge of the produced projectile fragment is determined from the etched track area distribution. Figure 3 shows the etched track area distribution of  $^{56}\text{Fe}$  and its fragments for a 462 A MeV  $^{56}\text{Fe}$  fragmentation on a  $\text{CH}_2$  target (target 2). The  $^{56}\text{Fe}$  beam and its fragments with charges of up to  $Z = 19$  are clearly shown as peaks. Other fragments with charges of less than  $Z = 20$  cannot be identified directly from the figure. Using seven Gaussian

**Fig. 2** (Color online) The track coordinate difference distribution of  $dx$  and  $dy$  for 497 A MeV  $^{56}\text{Fe}$  fragmentations on the  $\text{CH}_2$  target: (a), (b) are the differences between the front and back surfaces of the CR-39 sheet, respectively, and (c), (d) are the differences in front of and behind the target, respectively

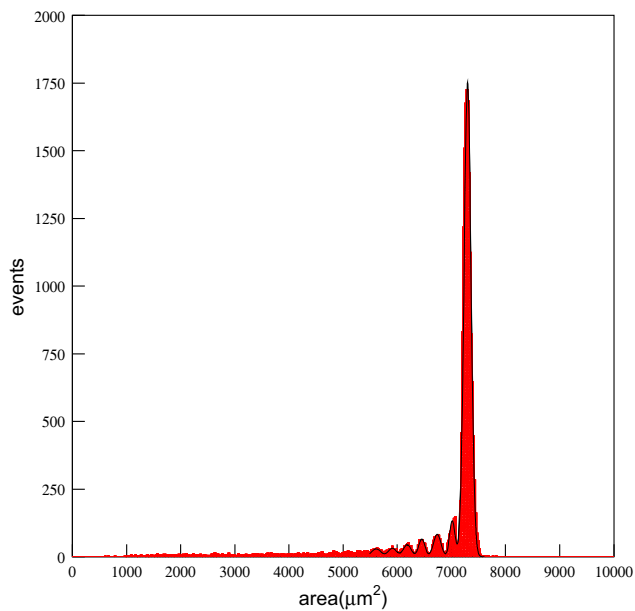
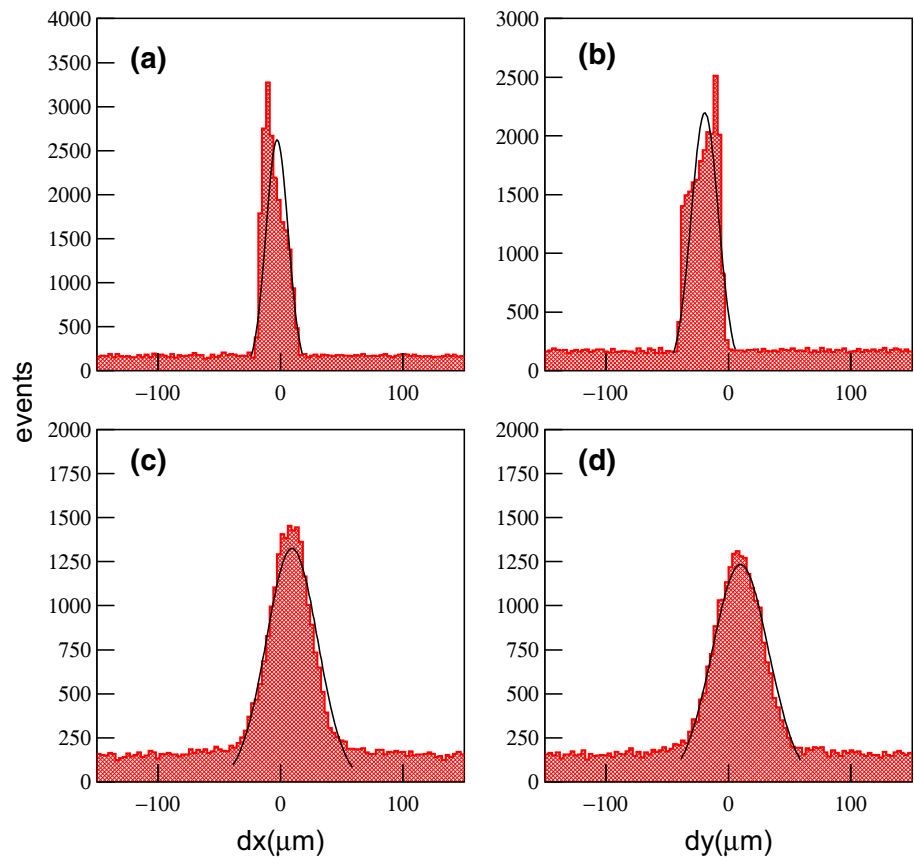


**Fig. 3** (Color online) The etched track area distribution of  $^{56}\text{Fe}$  and its fragments, for a 462 A MeV  $^{56}\text{Fe}$  fragmentation on  $\text{CH}_2$  targets, the smooth line represents the Gaussian fit

superposition fittings, we can obtain the mean etched track area and its deviation for  $^{56}\text{Fe}$  and its fragments with

charges greater than  $Z = 19$ . Figure 4 shows the dependence of the etched track area on the charge from the Gaussian-simulated results in Fig. 3, for  $^{56}\text{Fe}$  and its fragments with charges greater than  $Z = 19$ . The etched track area increases linearly with an increase in the charge ( $Z \geq 20$ ) of fragments up to the  $^{56}\text{Fe}$  beam charge. Using linear fitting, we find  $\text{Area} = 33.39 + 279.36Z$  with

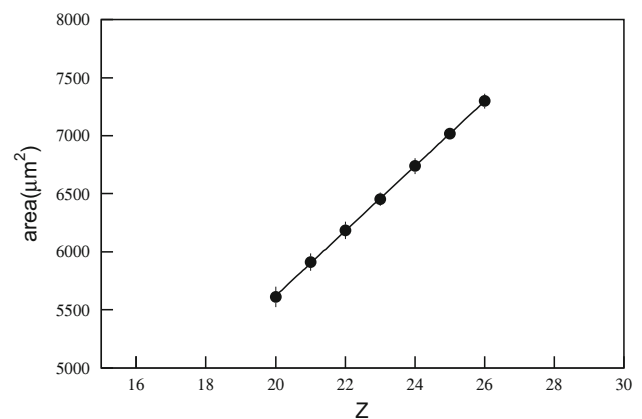


**Fig. 4** The dependence of the etched track area on the charge from the Gaussian-simulated results in Fig. 3, for  $^{56}\text{Fe}$  and its fragments with charges greater than  $Z = 19$

$\chi_{\min}^2 = 0.01$ . Based on this dependence, the charge of the other fragments can be determined.

Following the same procedure, the dependence of the etched track areas on the charge of the beam and fragments, for fragmentations of  $^{56}\text{Fe}$  on other targets, is given as follows:

$$\text{Area} = -242.54 + 280.01Z\chi_{\min}^2 = 0.06, 497\text{A MeV}^{56}\text{Fe} + \text{CH}_2 \quad (2)$$

$$\text{Area} = 83.71 + 267.29Z\chi_{\min}^2 = 0.04, 497\text{A MeV}^{56}\text{Fe} + \text{C} \quad (3)$$

$$\text{Area} = 53.10 + 266.83Z\chi_{\min}^2 = 0.03, 468\text{A MeV}^{56}\text{Fe} + \text{C} \quad (4)$$

$$\text{Area} = -232.68 + 279.74Z\chi_{\min}^2 = 0.23, 497\text{A MeV}^{56}\text{Fe} + \text{Al} \quad (5)$$

$$\text{Area} = 646.90 + 242.97Z\chi_{\min}^2 = 0.01, 478\text{A MeV}^{56}\text{Fe} + \text{Al} \quad (6)$$

Using the dependence of the etched track area on the charge of beams and fragments, for fragmentations of  $^{56}\text{Fe}$  on different targets at different beam energies, the charges of projectile fragments are identified. Figure 5 shows the projectile fragment etched track area distributions for fragmentations of  $^{56}\text{Fe}$  on different targets at different beam energies. The distribution with the highest peak is a fragment with charge  $Z = 25$ . Following the highest peak, the other peaks represent the distribution of projectile fragments with charges of  $Z = 24, 23, 22$ , and so on.

### 3 Results and discussion

The emission angles of PFs behind each target relate to the direction of the  $^{56}\text{Fe}$  ions before the target are determined using the coordinates of the  $^{56}\text{Fe}$  ions, the PFs, and the detector thickness. Track dimensions and positions within one microscope frame can be measured with an accuracy of  $\sim 0.1\ \mu\text{m}$ . However, the overall positional accuracy is dominated by the moving stage of the microscope. The positional uncertainty  $\sigma_p$  in the  $x$ - $y$  plane of the stack coordinate system is about  $3\ \mu\text{m}$ . The positional uncertainty  $\sigma_z$  in the  $z$ -axis comes from the stack composition and detector thickness measurements, and it is estimated as  $\sim 8\ \mu\text{m}$ . Using the quadruplet fitting method, the corresponding angular uncertainty is

$$\sigma(\theta) = \frac{\sqrt{\sigma_z^2 \sin^2 \theta + 2\sigma_p^2 \cos^2 \theta}}{2h}, \quad (7)$$

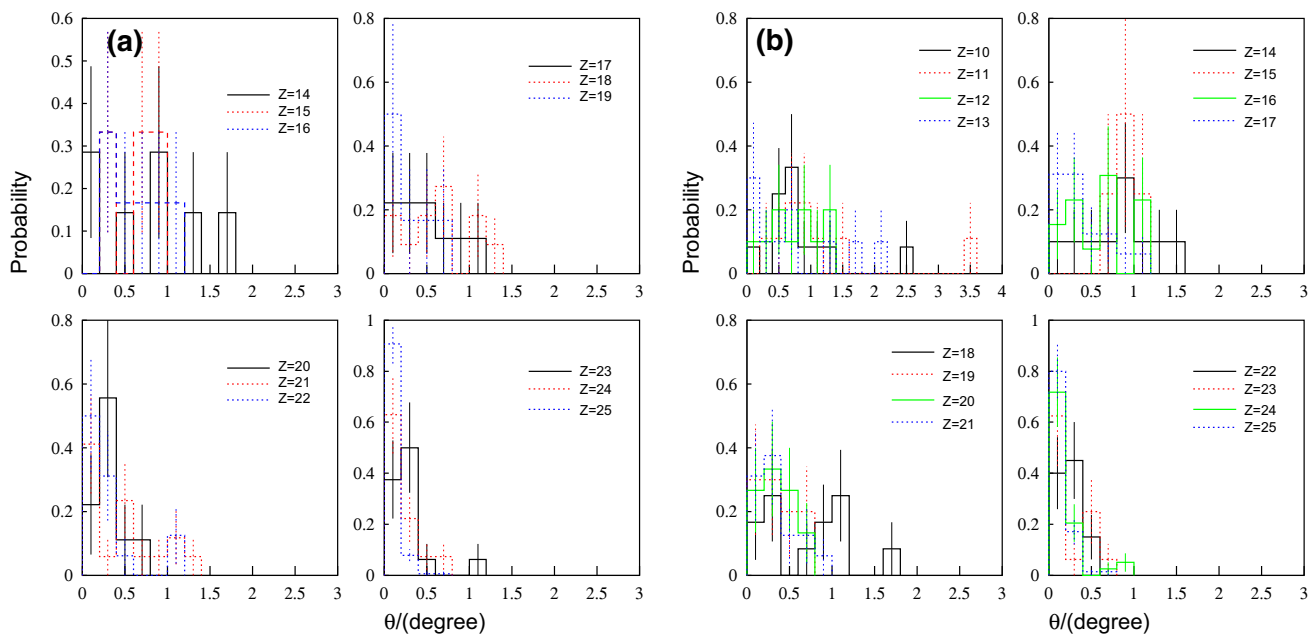
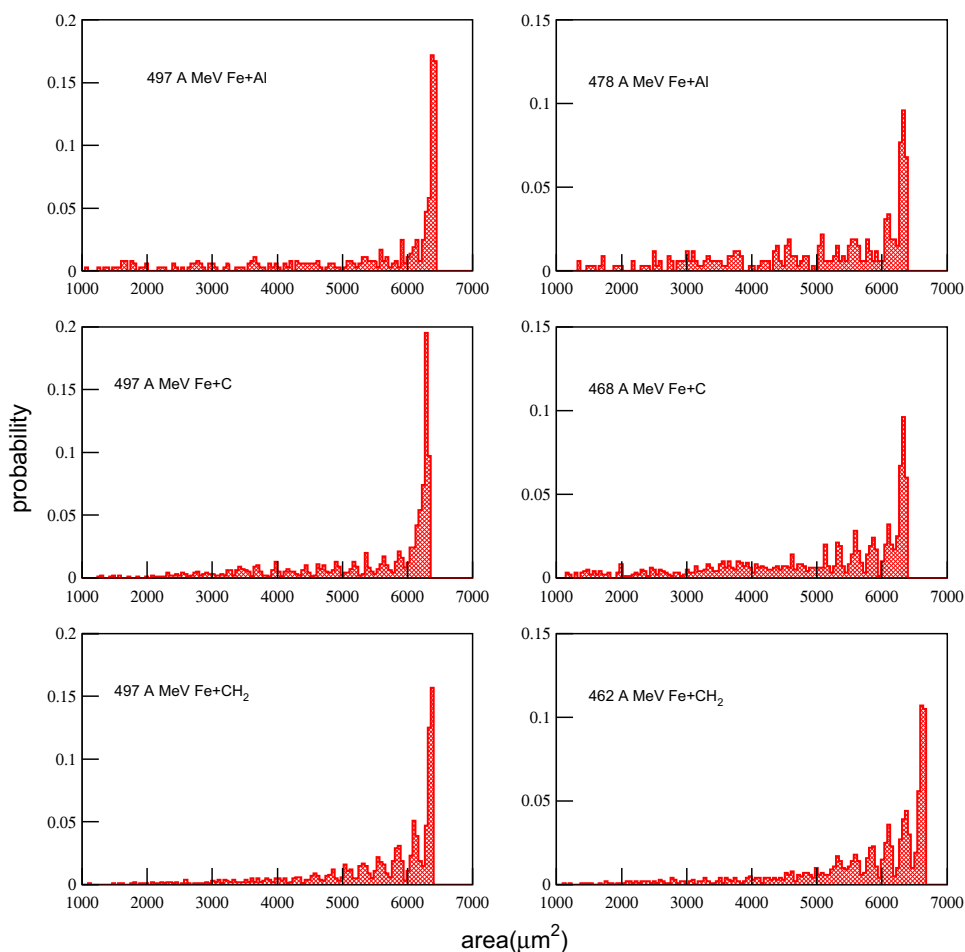
where  $\theta$  represents the polar angle of the fitted line. With a detector thickness of  $h = 780\ \mu\text{m}$ , we thus obtain angular uncertainties of  $\sigma(\theta) \approx 0.16^\circ$  for the value of  $\theta$  up to  $8^\circ$ . This angular uncertainty is not considered in the errors of the projectile fragment emission angle and scattering angle of beam particle measurements.

Figure 6 shows the angular distribution of PFs from the fragmentation of  $^{56}\text{Fe}$  on an Al target at 497 A MeV (a) and 478 A MeV (b). Figure 7 shows the angular distribution of PFs from the fragmentation of  $^{56}\text{Fe}$  on a C target at 497 A MeV (a) and 468 A MeV (b). Figure 8 shows the angular distribution of PFs from the fragmentation of  $^{56}\text{Fe}$  on a  $\text{CH}_2$  target at 497 A MeV (a) and 462 A MeV (b). The quoted errors in these figures are entirely statistical ones. From these figures, we can see that most PFs have an emission angle of less than 1.0 degree, though a few of them exceed 1.0 degree. With the decrease in the charges of the PFs, the angular distributions are widened. The angular distributions do not distinctly depend on the target mass for the same PF. The mean emission angles of PFs for  $^{56}\text{Fe}$  fragmentations on different targets at different energies are presented in Table 1, and the quoted errors are statistical ones. The mean emission angle distribution of PFs produced in fragmentations of  $^{56}\text{Fe}$  on different targets at different energies is shown in Fig. 9. It is found that the mean emission angle increases with the decrease in the charge of the PF, and no obvious beam energy and target size dependence are found in our studied beam energy region.

The transverse momentum per nucleon ( $p_t$ ) of a PF is calculated on the basis of its emission angle,  $p_t = p \sin \theta$ , where  $p$  is the momentum per nucleon of the beam, which can be calculated from the beam energy per nucleon ( $E$ ),  $p = \sqrt{E^2 + 2m_0E}$ , in which  $m_0$  is the nucleon rest mass.

A spectator is a part of the system which has not collided with the other nucleus, but which is nevertheless excited due to the shearing-off of part of the nucleus and the absorption of participant particles. The projectile spectators are identified as those particles that have an energy approximately identical to the beam energy per nucleon, but have a small reflecting angle relating to the beam direction. It was seen in Ref. [21] that they represent a well-equilibrated piece of nuclear matter at finite temperature. However, when the spectator is fully evolved, its properties are independent of incident energy, which supports the freeze-out picture [22]. The density and temperature remain approximately constant for several tens of fm/c, making it an ideal system to study the thermodynamic evolution of low-density, finite-temperature nuclear matter. According to the participant-spectator concept and the fireball model [23], if we assume that the emission of PFs is Maxwell-Boltzmann distributed in the projectile rest frame

**Fig. 5** (Color online) The etched track area distribution of projectile fragments for fragmentation of  $^{56}\text{Fe}$  on different targets at different beam energies



**Fig. 6** (Color online) The angular distribution of PFs from the fragmentation of  $^{56}\text{Fe}$  on Al targets at 497 A MeV (a) and 478 A MeV (b)

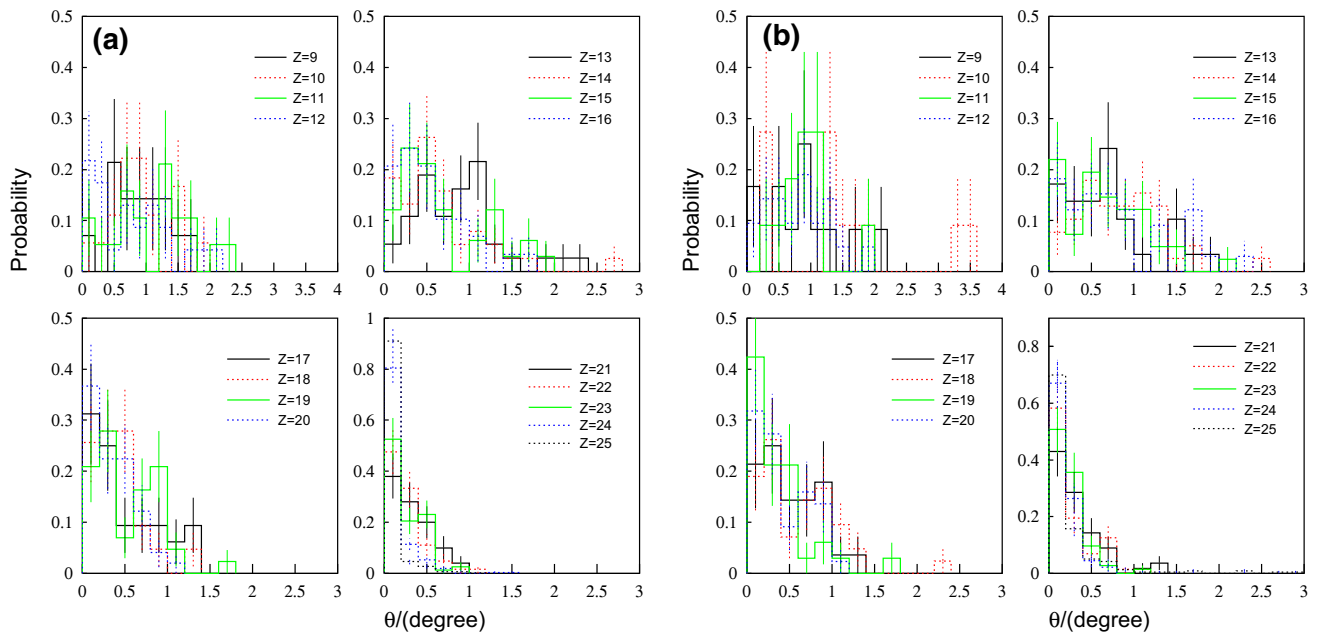


**Fig. 7** (Color online) The angular distribution of PFs from the fragmentation of  $^{56}\text{Fe}$  on C targets at 497 A MeV (a) and 468 A MeV (b)

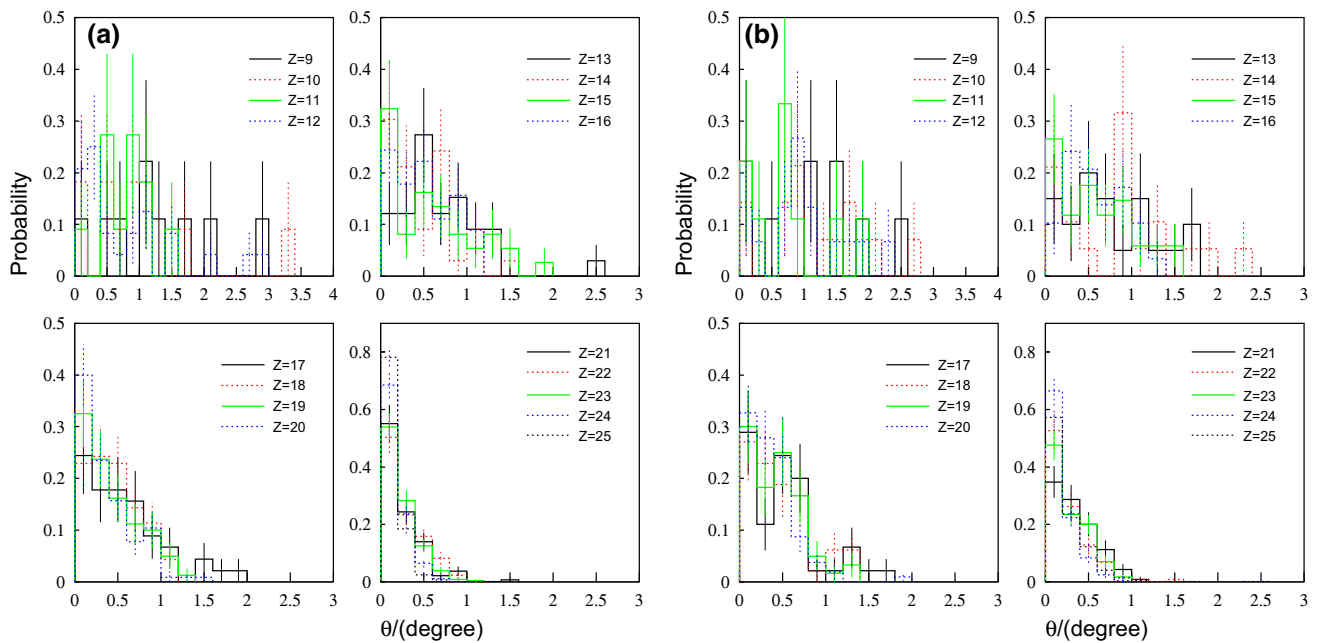


**Fig. 8** (Color online) The angular distribution of PFs from the fragmentation of  $^{56}\text{Fe}$  on  $\text{CH}_2$  targets at 497 A MeV (a) and 462 A MeV (b)

with a certain temperature  $T$ , then the integral frequency distribution of the squared transverse momentum per nucleon is

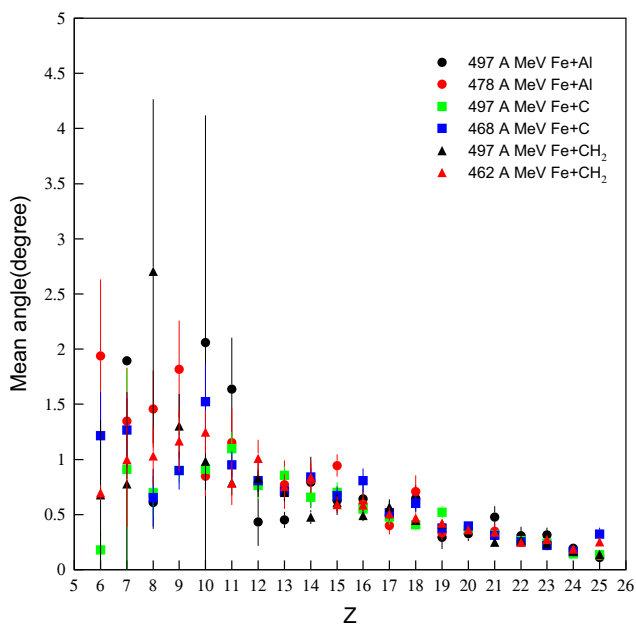
$$\ln F(> p_t^2) = -Ap_t^2/2m_p T \tag{8}$$

where  $A$  is the mass number of the PF and  $m_p$  is the proton mass. The linearity of such a plot would be strong evidence for a single temperature emission source. Figure 10 shows the cumulative plots of  $F$  as a function of  $p_t^2$  for PFs from

the fragmentation of  $^{56}\text{Fe}$  on Al targets at 497 A MeV (a) and 478 A MeV (b). Figure 11 shows the cumulative plots of  $F$  as a function of  $p_t^2$  for PFs from the fragmentation of  $^{56}\text{Fe}$  on C targets at 497 A MeV (a) and 468 A MeV (b). Figure 12 shows the cumulative plots of  $F$  as a function of  $p_t^2$  for PFs from the fragmentation of  $^{56}\text{Fe}$  on  $\text{CH}_2$  targets at 497 A MeV (a) and 462 A MeV (b). All of the plots can be fitted by a single Rayleigh distribution of the form

**Table 1** The mean emission angles(unit: degree) of PFs for  $^{56}\text{Fe}$  fragmentation on different targets at different energies(in parenthesis, unit: A MeV)

Charge of PFs	Al target		C target		CH <sub>2</sub> -target	
	$\langle\theta\rangle$ (497)	$\langle\theta\rangle$ (478)	$\langle\theta\rangle$ (497)	$\langle\theta\rangle$ (468)	$\langle\theta\rangle$ (497)	$\langle\theta\rangle$ (462)
Z = 25	0.109 ± 0.007	0.129 ± 0.013	0.137 ± 0.029	0.322 ± 0.061	0.139 ± 0.005	0.253 ± 0.022
Z = 24	0.196 ± 0.034	0.174 ± 0.034	0.144 ± 0.011	0.164 ± 0.015	0.168 ± 0.008	0.187 ± 0.011
Z = 23	0.315 ± 0.067	0.234 ± 0.056	0.244 ± 0.024	0.222 ± 0.023	0.235 ± 0.013	0.277 ± 0.016
Z = 22	0.307 ± 0.083	0.254 ± 0.033	0.266 ± 0.028	0.254 ± 0.031	0.269 ± 0.017	0.250 ± 0.021
Z = 21	0.478 ± 0.100	0.350 ± 0.064	0.318 ± 0.033	0.311 ± 0.040	0.248 ± 0.020	0.343 ± 0.023
Z = 20	0.325 ± 0.066	0.364 ± 0.046	0.363 ± 0.038	0.398 ± 0.044	0.360 ± 0.028	0.364 ± 0.028
Z = 19	0.294 ± 0.106	0.334 ± 0.070	0.522 ± 0.056	0.379 ± 0.061	0.414 ± 0.036	0.421 ± 0.042
Z = 18	0.646 ± 0.122	0.707 ± 0.150	0.407 ± 0.046	0.601 ± 0.071	0.449 ± 0.035	0.470 ± 0.051
Z = 17	0.494 ± 0.127	0.400 ± 0.082	0.479 ± 0.071	0.517 ± 0.062	0.568 ± 0.069	0.505 ± 0.062
Z = 16	0.644 ± 0.133	0.593 ± 0.105	0.551 ± 0.082	0.808 ± 0.108	0.492 ± 0.052	0.589 ± 0.062
Z = 15	0.629 ± 0.132	0.945 ± 0.100	0.701 ± 0.091	0.670 ± 0.077	0.608 ± 0.081	0.590 ± 0.076
Z = 14	0.792 ± 0.232	0.810 ± 0.151	0.656 ± 0.086	0.842 ± 0.084	0.478 ± 0.063	0.842 ± 0.148
Z = 13	0.451 ± 0.074	0.771 ± 0.222	0.855 ± 0.082	0.713 ± 0.092	0.702 ± 0.082	0.756 ± 0.112
Z = 12	0.432 ± 0.215	0.768 ± 0.118	0.763 ± 0.126	0.808 ± 0.103	0.828 ± 0.167	1.011 ± 0.168
Z = 11	1.638 ± 0.467	1.153 ± 0.307	1.099 ± 0.148	0.949 ± 0.123	0.789 ± 0.113	0.785 ± 0.199
Z = 10	2.059 ± 2.059	0.847 ± 0.180	0.910 ± 0.107	1.525 ± 0.336	0.983 ± 0.260	1.247 ± 0.195
Z = 9		1.816 ± 0.441	0.900 ± 0.113	0.900 ± 0.172	1.302 ± 0.291	1.167 ± 0.274
Z = 8	0.611 ± 0.239	1.459 ± 0.349	0.696 ± 0.216	0.654 ± 0.261	2.706 ± 1.559	1.031 ± 0.264
Z = 7	1.894 ± 0.006	1.347 ± 0.484	0.911 ± 0.911	1.268 ± 0.344	0.779 ± 0.779	0.997 ± 0.607
Z = 6		1.938 ± 0.695	0.180 ± 0.180	1.214 ± 0.399	0.678 ± 0.678	0.699 ± 0.067

**Fig. 9** (Color online) The dependence of mean emission angle on the charge of PFs for the fragmentation of  $^{56}\text{Fe}$  on different targets at different beam energies

$$F(> p_t^2) = C \exp(-p_t^2/2\sigma^2) \quad (9)$$

where  $\sigma = \sqrt{2/\pi}\langle p_t \rangle$ , which is related to the temperature of the PF emission source. Using the fitting parameter, the temperature of the PF emission source is calculated and is presented in Table 2. It is shown that the temperature of the PF emission source does not obviously depend on the target size. Generally, the temperature of the heavier PF emission source is less than that of the lighter PF emission source, but the difference is not distinct. The temperature of the PF emission source is about 1-8 MeV for the PFs with charges in the range from 9 to 25, which is in good agreement with the findings of Refs. [11–13, 16] based on isotope thermometers, but less than the result of Ref. [8] based on the PF kinetic energy spectrum.

The PFs are produced from the peripheral heavy-ion collisions, which provide an ideal scenario for studying the multi-fragment decay of hot and dilute nuclei. The PFs with a large charge  $Z$  or PFs with small charge  $Z$  come from projectile spectators. According to the participant-spectator concept [23], it is assumed that when the interaction between projectile and target nuclei takes place, both sweep out cylindrical cuts through each other. There is some intercommunication during the separation of the

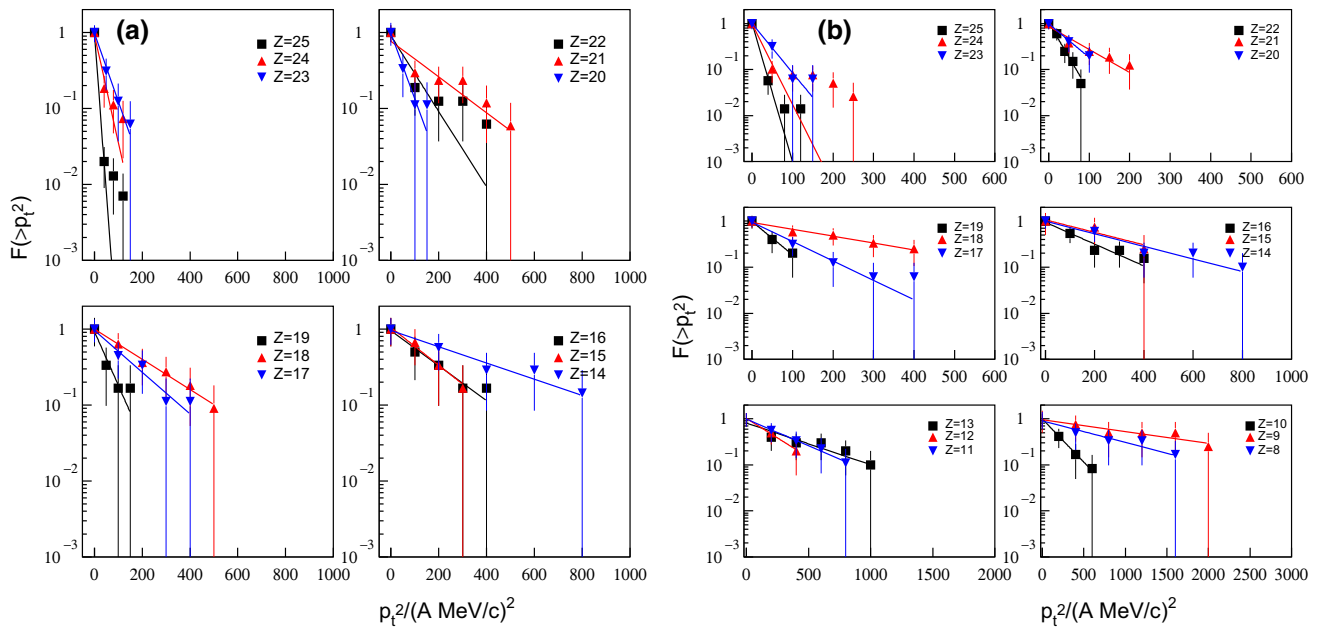


**Fig. 10** (Color online) The cumulative  $p_t^2$  distribution of PFs from the fragmentation of  $^{56}\text{Fe}$  on aluminum targets at 497 A MeV (a) and 478 A MeV (b)

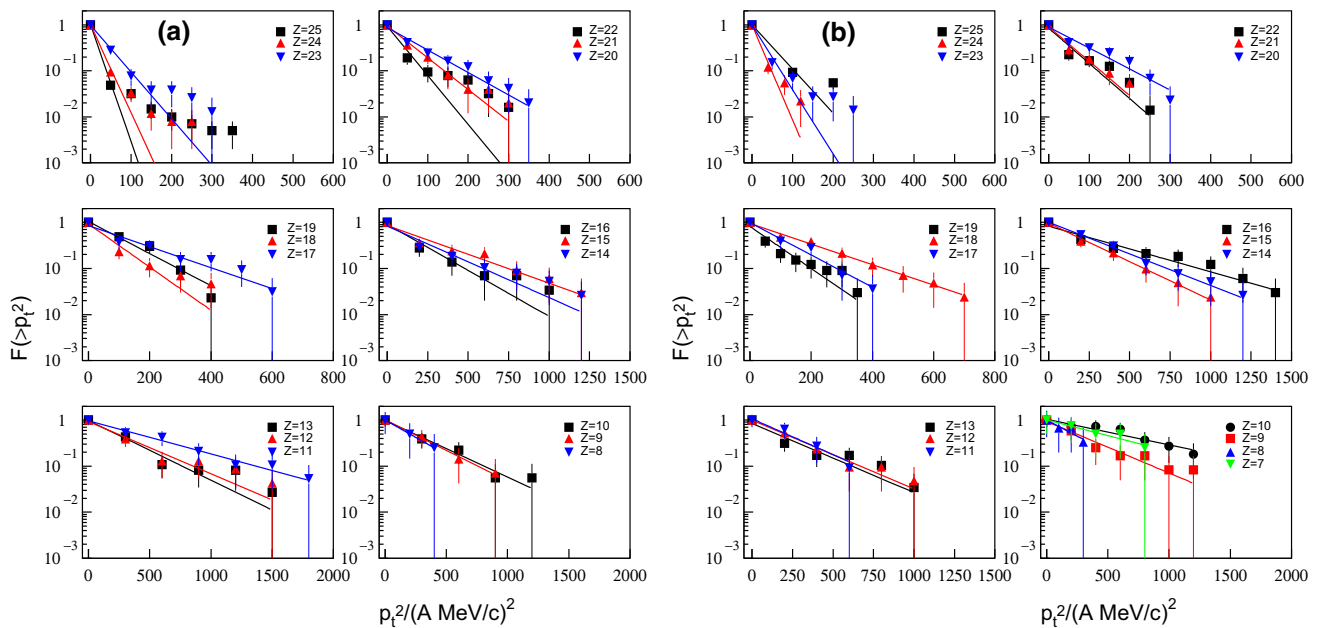


**Fig. 11** (Color online) The cumulative  $p_t^2$  distribution of PFs from the fragmentation of  $^{56}\text{Fe}$  on carbon targets at 497 A MeV (a) and 468 A MeV (b)

spectators and participants, which results in the excitation of the spectators. This excitation strongly depends on the contact area of the colliding system. The heavier fragments correspond to the large impact parameter and the small contact area, and the lighter fragments correspond to the smaller impact parameter and the larger contact area. Thus,

the excitation energy of the heavier fragments is less than that of the lighter fragments, resulting in the temperature of a heavier fragment's emission source being less than that of a lighter fragment's.

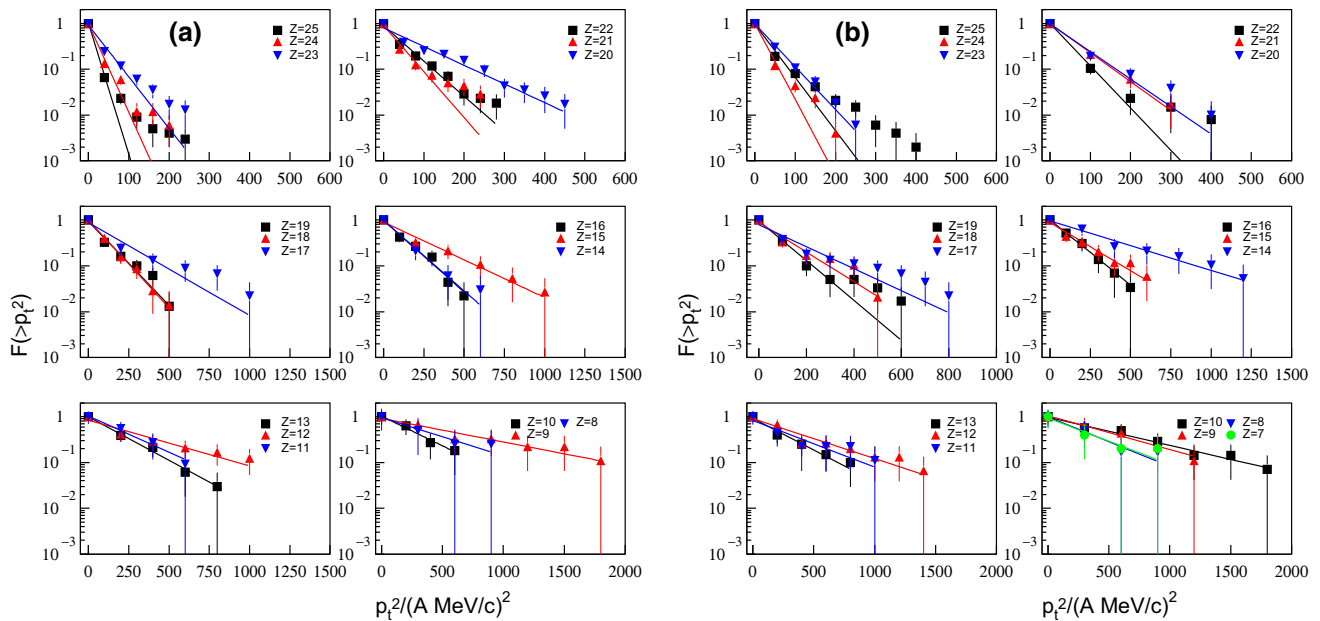


**Fig. 12** (Color online) The cumulative  $p_t^2$  distribution of PFs from the fragmentation of  $^{56}\text{Fe}$  on polyethylene targets at 497 A MeV (a) and 462 A MeV (b)

**Table 2** The temperature (unit: MeV) of the PF emission source for  $^{56}\text{Fe}$  fragmentations on different targets at different energies (in parenthesis, unit: A MeV)

Charge of PFs	Al target		C target		CH <sub>2</sub> -target	
	T (497)	T (478)	T (497)	T (468)	T (497)	T (462)
Z = 25	0.30 ± 0.04	0.43 ± 0.08	0.50 ± 0.04	1.33 ± 0.12	0.45 ± 0.02	1.10 ± 0.07
Z = 24	0.85 ± 0.24	0.69 ± 0.17	0.63 ± 0.06	0.59 ± 0.09	0.62 ± 0.05	0.73 ± 0.06
Z = 23	1.32 ± 0.38	1.10 ± 0.29	1.17 ± 0.15	0.85 ± 0.14	1.05 ± 0.09	1.27 ± 0.10
Z = 22	2.24 ± 1.05	0.74 ± 0.15	1.05 ± 0.22	1.46 ± 0.26	1.44 ± 0.12	1.21 ± 0.14
Z = 21	4.42 ± 1.51	2.07 ± 0.71	1.51 ± 0.23	1.40 ± 0.24	1.04 ± 0.12	1.65 ± 0.17
Z = 20	1.07 ± 0.43	1.27 ± 0.47	1.90 ± 0.27	2.03 ± 0.27	2.27 ± 0.20	1.55 ± 0.19
Z = 19	1.27 ± 0.74	1.24 ± 0.56	2.59 ± 0.32	1.98 ± 0.43	2.48 ± 0.30	2.07 ± 0.29
Z = 18	4.67 ± 1.37	6.21 ± 2.57	1.98 ± 0.42	4.16 ± 0.52	2.43 ± 0.26	2.87 ± 0.49
Z = 17	2.94 ± 1.06	1.92 ± 0.56	3.55 ± 0.66	2.31 ± 0.41	3.99 ± 0.88	3.38 ± 0.71
Z = 16	3.23 ± 1.59	3.13 ± 1.10	3.71 ± 0.91	7.46 ± 1.30	2.38 ± 0.30	2.61 ± 0.41
Z = 15	2.89 ± 1.36	5.30 ± 3.70	5.74 ± 1.05	4.31 ± 0.63	4.36 ± 0.77	3.42 ± 0.61
Z = 14	6.05 ± 2.77	4.74 ± 1.62	4.17 ± 0.93	4.73 ± 0.62	2.11 ± 0.43	5.98 ± 1.31
Z = 13		6.88 ± 2.85	4.82 ± 0.84	4.16 ± 1.04	3.29 ± 0.53	4.53 ± 1.23
Z = 12		3.29 ± 1.41	4.91 ± 1.24	3.72 ± 0.76	5.58 ± 1.50	6.40 ± 1.71
Z = 11		4.60 ± 1.65	7.39 ± 1.49	3.41 ± 1.00	3.37 ± 1.03	5.21 ± 2.48
Z = 10		2.47 ± 0.78	3.77 ± 0.87	8.35 ± 2.54	3.58 ± 1.29	7.52 ± 1.78
Z = 9		17.02 ± 12.24	3.32 ± 0.92	3.93 ± 1.19	8.52 ± 3.10	5.96 ± 1.93
Z = 8		7.91 ± 4.43	2.45 ± 1.86	2.66 ± 2.69	4.45 ± 3.24	3.41 ± 1.66
Z = 7				4.75 ± 3.26		3.20 ± 2.04

### 4 Conclusion

The emission angle distribution of PFs and the temperature of PF emission sources for fragmentations of  $^{56}\text{Fe}$  on C, Al, and CH<sub>2</sub> targets at different energies are studied using corrected data. It is found that the average emission

angle increases with the decrease in the charge of PF for the same target, and no obvious dependence of angular distribution on the mass of the target nucleus is found for the same PF. The cumulative squared transverse momentum distribution of PFs can be well represented by a single Rayleigh distribution. The temperature parameter of PF

emission sources is found to be about 1.0–8.0 MeV and does not depend on the mass of target for PFs with charges of  $9 \leq Z \leq 25$ . Generally, the temperature of heavier PF's emission sources is less than that of lighter PF's emission sources, but the difference is not distinct.

**Acknowledgements** We are grateful to staff of the HIMIC for helping to expose the stacks.

## References

1. A.S. Goldhaber, H.H. Heckman, High-energy interactions of nuclei. *Annu. Rev. Nucl. Part. Sci.* **28**, 161–205 (1978). <https://doi.org/10.1146/annurev.ns.28.120178.001113>
2. J. Pochodzalla, The search for the liquid-gas phase transition in nuclei. *Prog. Part. Nucl. Phys.* **39**, 443–501 (1997). [https://doi.org/10.1016/S0146-6410\(97\)00048-3](https://doi.org/10.1016/S0146-6410(97)00048-3)
3. N. Bohr, Neutron capture and nuclear constitution. *Nature (London)* **137**, 344–348 (1936). <https://doi.org/10.1038/137344a0>
4. G. Bertsch, P.J. Siemens, Nuclear fragmentation. *Phys. Lett. B* **126**, 9–12 (1983). [https://doi.org/10.1016/0370-2693\(83\)90004-7](https://doi.org/10.1016/0370-2693(83)90004-7)
5. W.A. Friedman, Rapid massive cluster function. *Phys. Rev. C* **42**, 667–673 (1990). <https://doi.org/10.1103/PhysRevC.42.667>
6. G.D. Westfall, B.V. Jacak, N. Anantaraman et al., Energy dependence of nuclear matter disassembly in heavy ion collisions. *Phys. Lett. B* **116**, 118–122 (1982). [https://doi.org/10.1016/0370-2693\(82\)90988-1](https://doi.org/10.1016/0370-2693(82)90988-1)
7. B.V. Jacak, G.D. Westfall, C.K. Gebke et al., Measurement of complex fragments and clues to the entropy production from 42 MeV/nucleon to 137 MeV/nucleon Ar + Au. *Phys. Rev. Lett.* **51**, 1846–1849 (1983). <https://doi.org/10.1103/PhysRevLett.51.1846>
8. T. Odeh, R. Bassini, M. Begemann-Blaich et al., Fragment kinetic energies and modes of fragment formation. *Phys. Rev. Lett.* **84**, 4557 (2000). <https://doi.org/10.1103/PhysRevLett.84.4557>
9. S. Wuenschel, A. Bonasera, L.W. May et al., Measuring the temperature of hot nuclear fragments. *Nucl. Phys. A* **843**, 1–13 (2010). <https://doi.org/10.1016/j.nuclphysa.2010.04.013>
10. S. Albergo, S. Costa, E. Costanzo et al., Temperature and free nucleon densities of nuclear matter exploding into light clusters in heavy-ion collisions. *Nuovo Cim. A* **89**, 1–28 (1985). <https://doi.org/10.1007/BF02773614>
11. V. Serfling, C. Schwarz, R. Bassini et al., Temperatures of exploding nuclei. *Phys. Rev. Lett.* **80**, 3928–3931 (1998). <https://doi.org/10.1103/PhysRevLett.80.3928>
12. J. Pochodzalla, T. Mohlenkamp, T. Rubehn et al., Probing the nuclear liquid-gas phase transition. *Phys. Rev. Lett.* **75**, 1040–1043 (1995). <https://doi.org/10.1103/PhysRevLett.75.1040>
13. W. Trautmann, R. Bassini, M. Begemann-Blaich, Thermal and chemical freeze-out in spectator fragmentation. *Phys. Rev. C* **76**, 064606 (2007). <https://doi.org/10.1103/PhysRevC.76.064606>
14. D.J. Morrissey, W. Benenson, E. Kashy et al., Excited state production and temperature measurement in a heavy ion reaction. *Phys. Lett. B* **148**, 423–427 (1984). [https://doi.org/10.1016/0370-2693\(84\)90730-5](https://doi.org/10.1016/0370-2693(84)90730-5)
15. C. Guo, S. Jun, F. Zhang, Comparison between nuclear thermometers in central Xe + Sn collision. *Nucl. Sci. Tech.* **24**, 050513 (2013). <https://doi.org/10.13538/j.1001-8042/nst.2013.05.013>
16. D.J. Morrissey, W. Benenson, W.A. Friedman, Measurement of temperature in nuclear reactions. *Annu. Rev. Nucl. Part. Phys.* **44**, 27–64 (1994). <https://doi.org/10.1146/annurev.ns.44.120194.000331>
17. D.-H. Zhang, L.-C. Wang, Y.-J. Li et al., Projectile fragmentation of 471 A MeV  $^{56}\text{Fe}$  in polyethylene, carbon and aluminum targets. *Radiat. Meas.* **50**, 56–60 (2013). <https://doi.org/10.1016/j.radmeas.2012.06.014>
18. D.-H. Zhang, L.-C. Wang, Y.-J. Li et al., Fragmentation  $^{56}\text{Fe}$  on C, Al and  $\text{CH}_2$  targets at 471 A MeV. *Nucl. Instrum. Methods B* **315**, 99–104 (2013). <https://doi.org/10.1016/j.nimb.2013.05.071>
19. Y.-J. Li, D.-H. Zhang, S.-W. Yan et al., Projectile fragment emission in the fragmentation of  $^{56}\text{Fe}$  on C, Al and  $\text{CH}_2$  targets at 471 A MeV. *Chin. Phys. C* **38**, 014001 (2014). <https://doi.org/10.1018/1674-1137/38/1/014001>
20. S. Ota, S. Kodaira, N. Yasuda et al., Tracking method for the measurement of projectile charge changing cross-section using CR-39 detector with a high speed imaging microscope. *Radiat. Meas.* **43**, S195–S198 (2008). <https://doi.org/10.1016/j.radmeas.2008.04.058>
21. C. Fuchs, P. Essler, T. Gaitanos et al., Temperature and thermodynamic instabilities in heavy ion collisions. *Nucl. Phys. A* **626**, 987–998 (1997). [https://doi.org/10.1016/S0375-9474\(97\)00467-3](https://doi.org/10.1016/S0375-9474(97)00467-3)
22. T. Gaitanos, H.H. Wolter, C. Fuchs, Spectator and participant decay in heavy ion collisions. *Phys. Lett. B* **478**, 79–85 (2000). [https://doi.org/10.1016/S0370-2693\(00\)00300-2](https://doi.org/10.1016/S0370-2693(00)00300-2)
23. G.D. Westfall, J. Gosset, P.J. Johansen et al., Nuclear fireball model for proton inclusive spectra from relativistic heavy ion collisions. *Phys. Rev. Lett.* **37**, 1202–1205 (1976). <https://doi.org/10.1103/PhysRevLett.37.1202>